Integrated Guidance, Navigation, and Control System Design for Active Debris Removal

Conings, V.A.B.; Mooij, E.

DOI
10.2514/6.2025-0085

Publication date
2025

Document Version
Final published version

Published in
AIAA Science and Technology Forum and Exposition, AIAA SciTech Forum 2025

AIAA SciTech Forum
6-10 January 2025, Orlando, FL
AIAA SCITECH 2025 Forum

10.2514/6.2025-0085

Integrated Guidance, Navigation, and Control System Design for Active Debris Removal

Vincent Conings* and Erwin Mooij †
Delft University of Technology, Faculty of Aerospace Engineering,
Kluyverweg 1, 2629 HS Delft, The Netherlands

Active debris removal missions are of paramount importance to mitigate the space debris problem around Earth. However, due to the complexity of such a debris removal mission, the first one is still to be launched. In particular, one critical technology enabler is presented by the guidance, navigation and control (GNC) system, as it is required to autonomously navigate around an uncontrolled and tumbling debris item. Therefore, the current paper is aimed at providing an integrated GNC system design to execute the final rendezvous with an uncooperative and passive debris object in low-Earth orbit (LEO). Specifically, it is focused on executing the most complex phase of an active debris removal mission, given in terms of its close-range rendezvous operations. The innovation of this paper lies in providing an end-to-end GNC system design, containing state of the art algorithms for the guidance, navigation, and control functions, along with the selection of appropriate navigation sensors and control actuators. Moreover, the proposed GNC system design showcases its autonomy and robustness by handing a wide variety of mission scenarios, while maintaining a terminal position accuracy at centimeter level and a limited propellant consumption. Furthermore, it is concluded that, as the developed GNC system design does not contain any intrinsic properties of its target, it can be employed during any generic active debris removal mission in LEO.

I. Introduction

To ensure long-term sustainable space operations, it is critical that humankind urgently acts to alleviate the debris problem faced in the direct vicinity around Earth. This is because a cascading effect, known as the Kessler syndrome [1], has already been initiated and when left undisturbed, will cause a chain reaction of collisions that results in an unbounded growth of space debris [2]. Therefore, to resolve this issue, active debris removal (ADR) missions have been proposed, as they provide the most effective solution strategy [3]. During such an ADR scenario, one or more resident space objects are removed from the most popular orbital regions around Earth. To execute such a complex mission, the development of an advanced guidance, navigation and control (GNC) system is necessary [4]. This is especially applicable for ADR missions targeted at uncooperative debris items with partially unknown mass and inertia properties. Moreover, these targeted debris objects are likely tumbling and not designed for rendezvous and docking with an active chaser spacecraft [5]. However, despite the pressing nature of the space debris issue, the first ever real ADR mission is still to be launched. Therefore, a strong incentive has recently been observed within the space industry, to control and mitigate this problem.

Examples related to this incentive are given by the e.Deorbit study performed by the European Space Agency (ESA) to remove the defunct Envisat satellite from orbit [6], as well as the ClearSpace-1 mission, currently being commissioned to perform a potential first deorbiting of a resident space object [7]. Furthermore, the Japanese ELSA-d mission provided commercial in-orbit demonstration of active debris removal technologies [8] and its successor, the Japanese ADRAS-J mission, is presently in orbit to characterise a Japanese upper stage, in preparation for a subsequent ADR mission [9]. However, not only the space industry has recently shown its interest. Also academia have performed extensive research, for example as given in [10], where an optimisation-based guidance system is developed for the autonomous final approach of a tumbling and non-cooperative target. Furthermore, Ref. [11] provides a partially integrated guidance and navigation system design that estimates the tumbling motion of an uncooperative target using Kalman filtering, while simultaneously applying a model predictive controller to execute the final approach of the target. The execution of the implemented control actions is, however, still assumed to be idealised.

*MSc Student, Section Astrodynamics and Space Missions, vincent.conings@gmail.com
†Associate Professor, Section Astrodynamics and Space Missions, e.mooij@tudelft.nl, Associate Fellow AIAA.

Therefore, the current paper is aimed at going one step further, by providing an integrated system design of the complete GNC system, including realistic sensor and actuator models. In particular, the paper provides a contribution in terms of a unified guidance, navigation, and control system tasked with performing an ADR mission to a defunct upper rocket body. A detailed analysis of each of the separate systems is provided, along with the integrated system performance. This contrasts with previous works, where idealised control and/or navigation systems have been employed.

The outline for the remainder of this paper is as follows. Section II discusses the mission scenario to the rocket body left in LEO-orbit. Subsequently, the relevant models that are implemented to simulate this mission are discussed in Sec. III. A discussion on the GNC system of the chaser is provided over three sections, where each subsystem is separately detailed. Firstly, the guidance subsystem is discussed in Sec. IV, after which Sec. V details the control subsystem of the chaser spacecraft. Thirdly, Sec. VI provides details on the developed navigation subsystem. Lastly, the paper provides the results that can be obtained with this integrated GNC system in Sec. VII and presents its conclusions in Sec. VIII.

II. Problem Definition

The ADR mission studied in the current paper consists of an active chaser spacecraft targeted at a defunct upper rocket body in a near-circular LEO-orbit. The implemented scenario is, however, limited to the study of the close-range rendezvous phase, as this phase is expected to be most complex in terms of GNC design. To perform the mission, the GNC algorithm of the chaser will autonomously provide onboard optimisation of the terminal rendezvous phase using convex optimisation, whereas the target is considered as uncooperative and passive. Furthermore, the target is assumed to be tumbling while traversing its orbit. A graphical representation of the implemented mission scenario is provided in Fig. 1, where it is expressed in two distinct reference frames. The first three mission phases can be described in the local-vertical-local-horizontal frame of the target, as it conveniently expresses the relative translational motion of its chaser spacecraft. Evidently, it is centred at the target spacecraft, with its X-axis pointing along the radial direction, its Y-axis pointing along the in-flight direction and its Z-axis complementing the right-handed frame by pointing perpendicular to the orbital plane. When using this frame to describe the relative motion between two spacecraft, however, it is also commonly referred to as the Hill frame and its reference directions are then defined as R-bar, V-bar and H-bar, respectively. The remaining two mission phases are conveniently expressed with respect to the body frame of the target spacecraft, given by the $X_{B,T}$, $Y_{B,T}$ and $Z_{B,T}$ reference directions, as both the relative

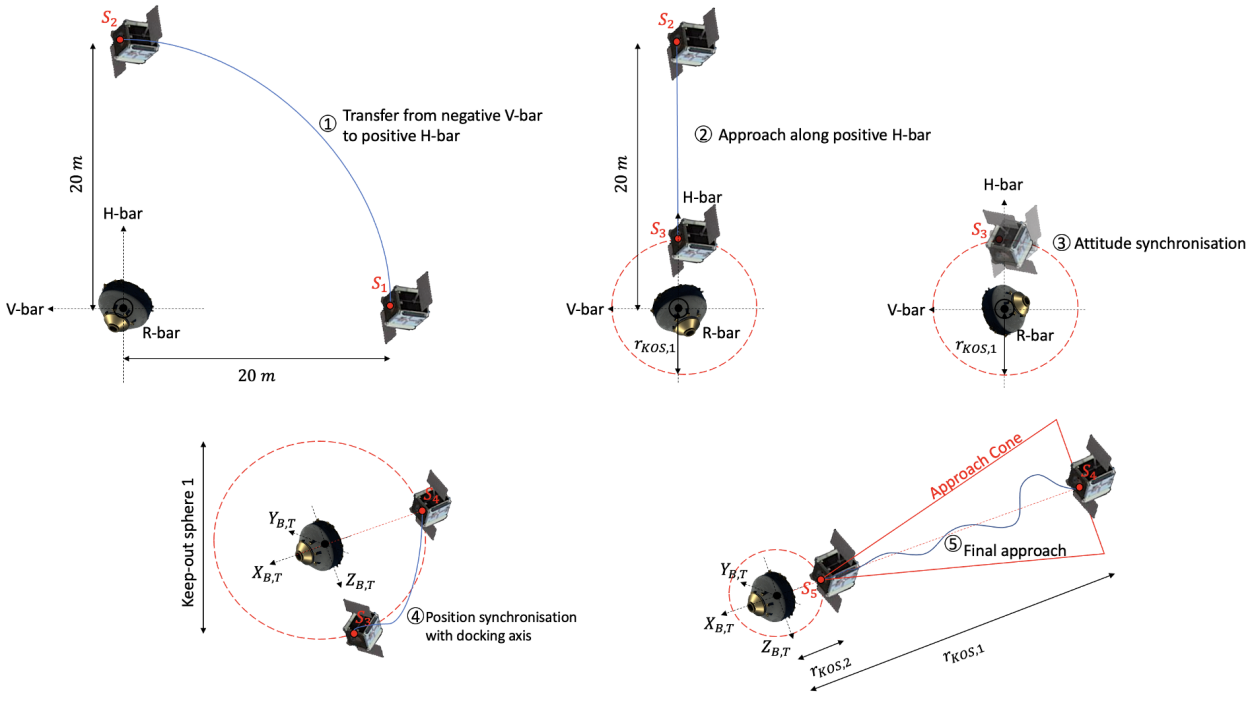

Fig. 1 Mission scenario definition. Figure adapted from [12] and [13].

translational and rotational motion of the chaser are to be considered.

The sequence of mission phases starts with a transfer from a hold point S_1, on the negative V-bar of the target's Hill frame, to a hold point S_2, on its positive H-bar. This approach direction is considered as safest, given that the rocket body is likely in a flat spin. This is a reasonable assumption when considering that internal dissipation will always transform arbitrary rotations to a flat spin within a relatively short time span of approximately one year [14]. Subsequently, the chaser approaches the target along its H-bar axis from hold point S_2 to hold point S_3, while remaining outside of the first keep-out sphere with radius $r_{KOS,1}$. Note that this approach is necessary prior to synchronisation with the motion of the tumbling docking-axis of the target, as the chaser will have limited thrusting capabilities to compensate the centrifugal forces encountered during this manoeuvre. For the third mission segment, the chaser spacecraft performs attitude synchronisation with the tumbling target, while maintaining its position at hold point S_3. Then, prior to approaching the passive target along its docking-axis in the final approach phase, the chaser spacecraft synchronises its position with it. Hence, during this phase, the chaser transfers from hold point S_3, on the positive H-bar of the target, to a hold point S_4 along the instantaneous direction of the docking-axis. Subsequently, the final approach phase between hold points S_4 and S_5 is initiated and the inter-satellite distance is reduced. This is achieved while simultaneously remaining outside the second keep out sphere with radius $r_{KOS,2}$ and maintaining position and attitude synchronisation.

The considered mission scenario thus starts with the chaser at hold point S_1 and ends with the chaser located at capture position S_5. During this entire mission scenario, the approach velocity of the chaser is limited to 1 m/s to ensure low impact docking and a keep-out sphere of variable size is imposed around the target.

III. Model Definition

The reference frames employed in this paper are given by the inertial frame, the Hill frame and the spacecraft body frame. The selected implementation of the inertial frame is the Earth-Centred EME2000 frame and the translational dynamics of the chaser and target spacecraft within this frame are given by:

$$\mathbf{a} = \frac{\mathbf{F}_{net}}{m} \tag{1}$$

This representation is a Cartesian form of the translational state dynamics of each satellite in orbit. In this equation, $\mathbf{a}$ is defined as the acceleration vector, $\mathbf{F}_{net}$ as the net external force vector, and m the instantaneous mass. The modelled environmental forces that make up $\mathbf{F}_{net}$ are given by: gravity acceleration due to a spherical harmonic Earth with degree and order 2, atmospheric drag acceleration, and solar-radiation-pressure acceleration.

The rotational motion of both spacecraft is modelled using Euler's equation for rigid body dynamics:

$$\dot{\boldsymbol{\omega}} = \mathbf{J}^{-1} \left(\mathbf{M}_{net} - \boldsymbol{\omega} \times \mathbf{J}\boldsymbol{\omega} \right) \tag{2}$$

In this equation, $\boldsymbol{\omega}$ represents the angular velocity vector of the body, $\mathbf{J}$ its instantaneous inertia tensor and $\mathbf{M}_{net}$ the net external moment vector acting on the body. The modelled environmental torques that make up $\mathbf{M}_{net}$ are given by: gravity gradient torque due to a spherical harmonic Earth with degree and order 2, atmospheric drag torque, solar-radiation-pressure torque, and magnetic-dipole torque. In addition to this, the kinematic attitude is modelled in terms of the quaternion vector $\mathbf{q}$, as given by:

$$\dot{\mathbf{q}} = \frac{1}{2} \begin{bmatrix} q_4 & -q_3 & q_2 \\ q_3 & q_4 & -q_1 \\ -q_2 & q_1 & q_4 \\ -q_1 & -q_2 & -q_3 \end{bmatrix} \boldsymbol{\omega} \tag{3}$$

Note that the relevance of the provided acceleration and torque models has been determined from a mission analysis. During this analysis, the magnitude of the relative translational and rotational state errors between the spacecraft have been obtained for each environmental disturbance. Using a simulation time of six hours, selected to account for contingency conditions during mission execution, resulted in the previously provided environmental disturbances.

The relative translational dynamics between the chaser spacecraft and its target are modelled using the linear Hill equations. This is done as the implemented mission scenario ensures that the distance between both spacecraft is small, especially in comparison with the distance to the central body, and that the target orbit is near-circular. As such, the assumptions of the Hill model are satisfied and the simplified linear model can be applied. This model expresses the

relative dynamics of the chaser with respect to its target in the Hill frame [15] and consists of the following system of linearised differential equations:

$$\begin{cases} \ddot{x} - 2n\dot{y} - 3n^2 x = f_x \\ \ddot{y} + 2n\dot{x} = f_y \\ \ddot{z} + n^2 z = f_z \end{cases} \tag{4}$$

In these equations, x, y and z represent the three position components of the chaser relative to its target. Moreover, n represents the mean motion of the target's orbit and f_x, f_y and f_z represent the components of the force per unit mass acting on the spacecraft, external to the Newtonian gravity of the main body.

When defining the translational state vector of the chaser spacecraft as $\mathbf{x} = (\mathbf{r}, \mathbf{V})^T$, Eq. (4) can be rewritten into Eqs. (5) and (6), and used as model for the system dynamics onboard the guidance system.

$$\dot{\mathbf{r}}(t) = \mathbf{V}(t) \tag{5}$$

$$\dot{\mathbf{V}}(t) = \begin{bmatrix} 0 & 2n & 0 \\ -2n & 0 & 0 \\ 0 & 0 & 0 \end{bmatrix} \mathbf{V}(t) + \begin{bmatrix} 3n^2 & 0 & 0 \\ 0 & 0 & 0 \\ 0 & 0 & -n^2 \end{bmatrix} \mathbf{r}(t) + \frac{\mathbf{T}(t)}{m} \tag{6}$$

In Eq. (6), $\mathbf{T}$ represents the thrust vector generated by the chaser spacecraft and m represents its mass. Therefore, to limit the complexity of the onboard dynamics, any perturbations in the external force vector are omitted and $(f_x, f_y, f_z)^T = \frac{\mathbf{T}(t)}{m}$. Furthermore, as the fuel consumption during the final approach phase is expected to be low, also mass dynamics are omitted in the onboard guidance model. Lastly, it is assumed that omnidirectional thrust is available, such that only translational motion guidance needs to be performed and simplified guidance algorithms can be obtained [10]. Consequently, the rotational motion guidance can be decoupled and attitude synchronisation will be maintained as an attitude control problem. As such, Eqs. (5) and (6) contain the entire system model implemented onboard the guidance system.

IV. Guidance System

In this paper, the guidance system of the chaser spacecraft is developed to solve consecutive trajectory optimisations of the mission scenario, as previously established in Fig. 1. A summary of this implemented guidance system is provided in Fig. 2. Note that, for each of the five phases of the mission scenario, a separate guidance scheme is followed. For the transfer guidance phase 1, the approach guidance phase 2, the position synchronisation guidance phase 4 and the final approach guidance phase 5, a numerical guidance scheme based on convex optimisation is employed. This is in contrast with the guidance scheme applied to the attitude synchronisation phase, given as phase 3, as it consists of a simple tracking guidance system that maintains proximity with hold point S_3. Note again that, due to the availability of omnidirectional thrust, the guidance system has been decoupled from the attitude control system and is therefore only required to provide position tracking of the hold point. As a result, the current mission phase can be executed using a much simpler tracking guidance system design. Nevertheless, to enhance robustness of the developed guidance methodology, the tracking guidance system is also enabled during phase 1, 2, 4 and 5, along with the convex guidance system. This is done to maintain proximity with the reference trajectory. Note that this reference trajectory is frequently recalculated using the current state of the chaser as initial condition and, in case an infeasible solution is encountered, the convex guidance system no longer outputs thrust commands. Instead, it outputs the last feasible reference trajectory it obtained such that the tracking system can guide the chaser back to a point where the convex problem formulation is feasible.

For the convex guidance system, a separate definition of the optimisation problem is applicable to each of the four considered mission phases. However, as these optimisation problems are rather similar, but not identical, a general problem definition is provided here. This general optimisation problem is subsequently implemented per mission segment, with different parameter values for the constraint equations.

The general convex optimisation problem solved by the guidance system is provided in Problem 1, where the objective is to minimise the cumulative thrust force over the given mission segment, as described by Eq. (7).

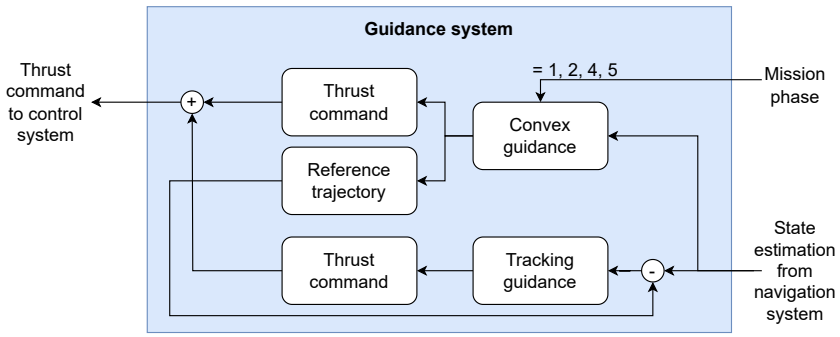

Fig. 2 Guidance system design

Problem 1:

$$\underset{\mathbf{T}(t),\mathbf{r}(t),\mathbf{V}(t)}{\text{minimise}} \quad J_f = \int_0^{t_f} ||\mathbf{T}(t)||dt \quad \text{subject to} \tag{7}$$

$$\dot{\mathbf{r}}(t) = \mathbf{V}(t) \tag{8}$$

$$\dot{\mathbf{V}}(t) = \begin{bmatrix} 0 & 2n & 0 \\ -2n & 0 & 0 \\ 0 & 0 & 0 \end{bmatrix} \mathbf{V}(t) + \begin{bmatrix} 3n^2 & 0 & 0 \\ 0 & 0 & 0 \\ 0 & 0 & -n^2 \end{bmatrix} \mathbf{r}(t) + \frac{\mathbf{T}(t)}{m} \tag{9}$$

$$\boldsymbol{\eta}^T(t)\mathbf{r}(t) \geq r_{KOS} \tag{10}$$

$$||\mathbf{V}(t)|| \leq V_{max} \tag{11}$$

$$0 \leq |\mathbf{T}_x(t)| \leq T_{max} \tag{12}$$

$$0 \leq |\mathbf{T}_y(t)| \leq T_{max} \tag{13}$$

$$0 \leq |\mathbf{T}_z(t)| \leq T_{max} \tag{14}$$

$$\mathbf{r}(0) = \mathbf{r}_0 \quad \mathbf{V}(0) = \mathbf{V}_0 \tag{15}$$

$$\mathbf{r}(t_f) = \mathbf{r}_f \quad \mathbf{V}(t_f) = \mathbf{V}_f \tag{16}$$

Furthermore, the dynamics of the system are provided in terms of the linear Hill equations Eqs. (8) and (9). As a common safety precaution, the reference trajectory of the chaser must remain outside a keep-out sphere, given by Eq. (10), and the maximum transfer velocity is constrained by Eq. (11). Note that a keep-out sphere constraint by itself is a non-convex constraint and is currently given in a convexified form by utilising the rotating-hyperplane method, as proposed in [10]. This method, instead of enforcing a spherical keep-out zone, applies a rotating plane to confine the design space to a moving half-space outside the keep-out sphere. Hence, for the rotating-hyperplane method to mimic a keep-out sphere constraint, the dividing plane must rotate along with the position of the spacecraft in its reference trajectory, as given in Fig. 3.

In this figure, the left side depicts a conventional keep-out sphere constraint, whereas the right side contains the rotating-hyperplane method. Note that for intuitive interpretation, the rotating-hyperplane is applied to a two-dimensional reference scenario, but the methodology is evidently not limited to two-dimensional problems. Furthermore, note that in this figure, three instances of the rotating-hyperplane are provided and each one is activated separately, rather than jointly. Mathematically, the rotation of this hyperplane can be defined by the vector $\boldsymbol{\eta}(t)$, which represents the time history of the outward unit normal of the separating plane and will be defined per mission segment.

Furthermore, Eqs. (12) to (14) constrain the thrust-vector history to the performance characteristics of the onboard engines. As omnidirectional thrust is available, the magnitude of the thrust vector can simply be constrained along its three scalar components. Lastly, the initial state is applied in Eq. (15) and the final state in Eq. (16).

The optimisation problem defined in Problem 1 is directly applicable as transfer guidance, approach guidance and synchronisation guidance, each with their own parameters to define the constraint equations. Furthermore, it is also applicable as final approach guidance, but needs to be extended with two additional convex trajectory constraints. First, to ensure a more accurate tracking of the docking-axis, an additional constraint is imposed in the form of an approach cone with predefined half angle. A mathematical description of this approach cone constraint is provided by:

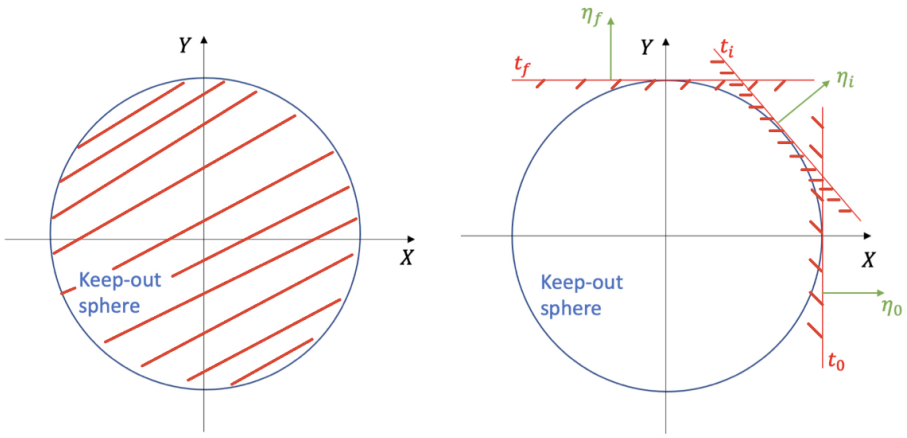

Fig. 3 Conventional keep-out sphere constraint represented by hatched area (left) and rotating-hyperplane constraint represented by hatched half-spaces (right)

$$||\mathbf{r}(t)|| \cos\alpha \leq \mathbf{e}_d(t) \cdot \mathbf{r}(t) \tag{17}$$

where α represents the half-angle of the approach cone and $\mathbf{e}_d(t)$ the instantaneous definition of the tumbling docking axis in the Hill frame of the target. Secondly, a keep-in sphere constraint is imposed during final approach to limit the magnitude of the position vector and is given by:

$$||\mathbf{r}(t)|| \leq r_{max} \quad \text{where} \quad \begin{cases} r_{max} = ||\mathbf{r}_0|| & \text{if} \quad ||\mathbf{r}_0|| > r_{KOS,2} \\ r_{max} = 5 & \text{if} \quad ||\mathbf{r}_0|| \leq r_{KOS,2} \end{cases} \tag{18}$$

This keep-in sphere constraint is defined such that a forced-motion manoeuvre towards the docking position is obtained, where the maximum radial position is constrained by the magnitude of the initial position, $||\mathbf{r}_0||$. This ensures a reference trajectory along the direction of the capture position, instead of a combined outward-inward manoeuvre. Nevertheless, in case navigation and/or control errors cause the initial position to lie within the keep-out sphere region, the maximum allowed radial distance to the target is modified to 5 m. This is done to allow the spacecraft to leave the second keep-out sphere and increase the inter-satellite distance, but not further than the base plane of the approach cone.

Furthermore, for the tracking guidance system, first analyses showed that a simple PD controller is sufficient to perform hold-point tracking during attitude synchronisation, as well as reference trajectory tracking in between recalculations of the convex guidance system. The error that is tracked by this controller is expressed in terms of the trajectory error, *i.e.*, the discrepancy between the reference trajectory calculated by the guidance system and the current position estimated by the navigation system.

A summary of the parameter values defining the guidance system is provided in Table 1.

As a result of the provided convex guidance system design, the trajectory of Fig. 4 can be obtained. Note that the transfer and approach phases of the mission scenario are provided in the Hill frame, whereas the synchronisation and final approach phases are expressed in the body frame of the target. Furthermore, the attitude synchronisation phase is provided in both frames to indicate this frame transition. From the figure it can be seen that a successfull reference trajectory is provided that transfers from the negative V-bar to the positive H-bar, approaches along the H-bar up to the first keep-out sphere constraint, and maintains this hold-point for attitude synchronisation. Subsequently, the trajectory synchronises its position with the docking-axis of the target, represented by the dotted black line, after which it approaches the target within the approach cone up to the second keep-out sphere. The provided reference trajectory ensures that no path constraints are violated and that the established mission scenario can successfully be executed.

Furthermore, when integrating the convex guidance scheme with the tracking guidance algorithm into an overall subsystem, the performance of Fig. 5 can be obtained. In this figure, a comparison is provided between the reference trajectory of the convex guidance algorithm, indicated by the green curve, and the simulated trajectories with and without tracking guidance, as indicated by the blue and red curves, respectively. Note that these simulated trajectories are obtained by modelling the orbital disturbances previously discussed in Sec. III.

Table 1 Parameter values of guidance system

Time step of guidance function Δt_{guid} [s]	1
Chaser mass m [kg]	500
Mean motion of target orbit n [deg/s]	0.063
Maximum approach velocity V_{max} [m/s]	1
Maximum thrust level T_{max} [N]	220
Keep-out sphere radius during transfer, approach and synchronisation phases $r_{KOS,1}$ [m]	5
Keep-out sphere radius during final approach $r_{KOS,2}$ [-]	1.35
Approach cone half-angle α [deg]	30
Tracking guidance K_p [-]	50
Tracking guidance K_d [-]	200

It can be seen that the simulation with tracking guidance is capable of closely following the reference, resulting in a near-zero trajectory error throughout the entire mission duration, whereas the trajectory without tracking guidance starts to disperse from the reference during the attitude synchronisation phase. This is because disturbances cause the chaser to drift away from hold point S_3, rendering the convex guidance system incapable of calculating commands during the subsequent position synchronisation phase and final approach phase. Hence, it is clear that the implementation of the tracking guidance system is absolutely necessary.

Lastly, the thrust commands calculated by the combined guidance system are provided in Fig. 6. From this figure it can be concluded that the required control input remains bounded and no extended periods of actuator saturation are commanded.

V. Control System

The control system of the chaser spacecraft calculates the commands needed to maintain attitude synchronisation between the target and chaser during close-range rendezvous. The developed control system will thus only control the rotational motion of the chaser, whereas the translational motion is controlled by executing the commands provided by the guidance system. This implies that the translational and rotational motion of the chaser are decoupled, reducing the complexity of both systems.

The implemented control algorithm is summarised in Fig. 7 and consists of two consecutive controllers, a linear P controller and a full state Incremental Nonlinear Dynamic Inversion (INDI) controller, as has been applied in Ref. [16]. This is done as the direct use of a full state attitude controller for synchronisation with a tumbling target will be inefficient. An instability is caused by the fact that, for complete synchronisation, both the angular velocity and instantaneous attitude must be matched with the debris item. However, errors in the instantaneous attitude synchronisation will drive the controller to corrective actions, causing a divergence from rate synchronisation. Conversely, errors in rate synchronisation will force the controller to different corrective actions, causing a divergence from instantaneous attitude synchronisation. Therefore, a straightforward proportional controller is proposed to achieve rate synchronisation to within a given threshold, after which simultaneous attitude and angular velocity synchronisation is achieved using a full state INDI controller. Note that, the INDI controller is selected as robust attitude controller, due to its capability of handling nonlinear dynamics without the need of having a detailed system model. In fact, the INDI controller obtains detailed knowledge on the system through measurements of the spacecraft state and control actuator output and uses this knowledge to cancel out nonlinearities in the uncertain system model. As a result, a robust and straightforward methodology can be used to effectively control a complex system.

A mathematical description of this attitude control system is given below in Problem 2.

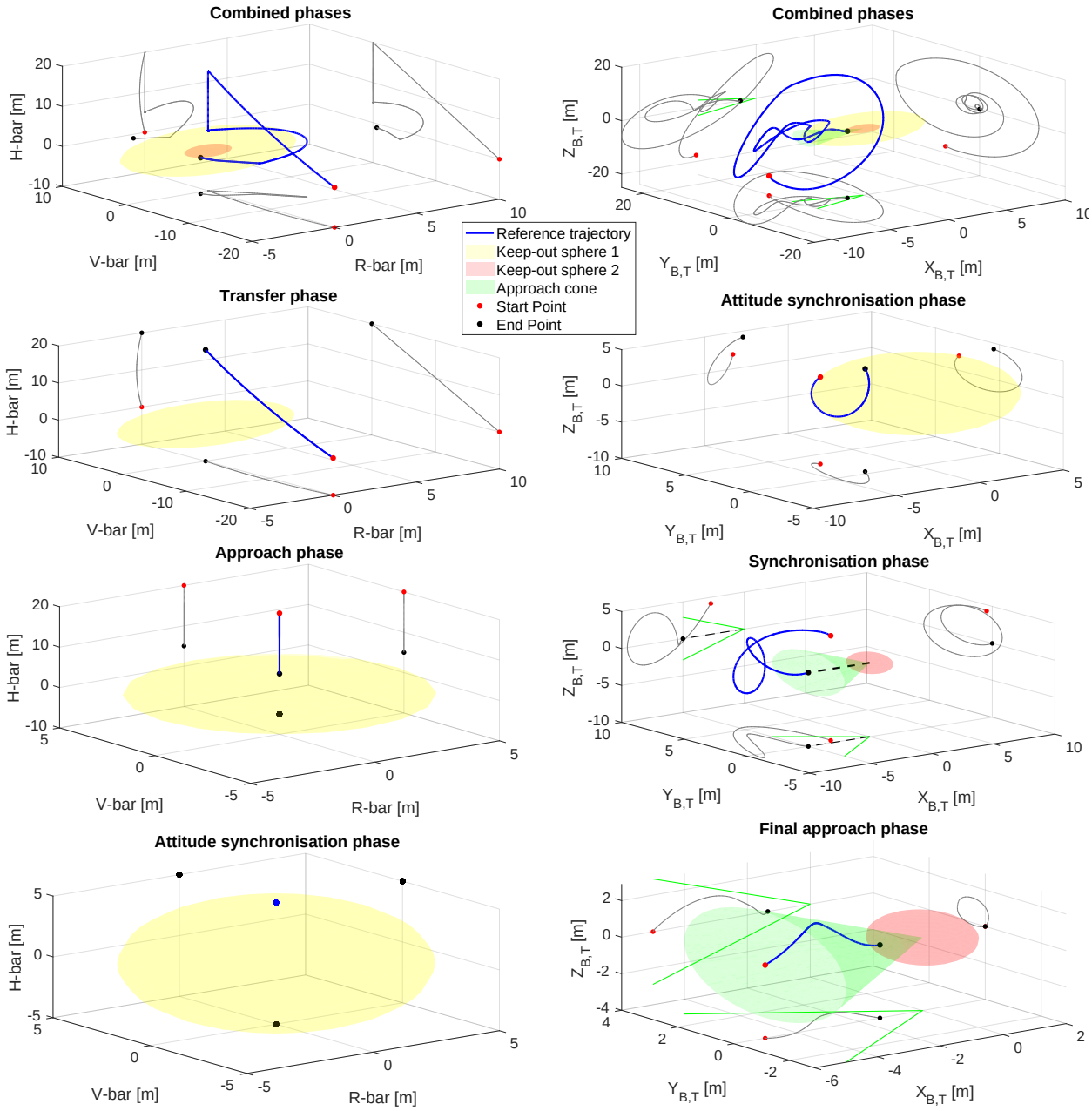

Fig. 4 Reference trajectory provided by the convex guidance system, as expressed in the Hill frame of the target spacecraft (left) and its body frame (right), with keep-out sphere and approach cone constraints

Problem 2:

$$\text{if } \|\Delta\boldsymbol{\omega}\| > 0.6 \text{ deg/s}:$$

$$\mathbf{M} = K_p\left(\boldsymbol{\omega}_T - \boldsymbol{\omega}_C\right) \tag{19}$$

else:

$$\mathbf{M} = \mathbf{M}_0 + \mathbf{J}\left(K_{p,in}\left(\boldsymbol{\omega}_{des} - \boldsymbol{\omega}_C\right) - \dot{\boldsymbol{\omega}}_{meas}\right) \tag{20}$$

$$\boldsymbol{\omega}_{des} = -\left(\mathbf{Q}_2\right)^T\left(2\mathbf{Q}_1\mathbf{Q}_1^T K_{p,out}\left(\Delta\mathbf{q}\right) - \mathbf{Q}_1\boldsymbol{\omega}_T\right) \tag{21}$$

$$\Delta\mathbf{q} = \begin{cases} \begin{pmatrix}0 & 0 & 0 & 1\end{pmatrix}^T - \delta\mathbf{q} & \text{if} \quad \delta q_4 \geqslant 0 \\ \begin{pmatrix}0 & 0 & 0 & -1\end{pmatrix}^T + \delta\mathbf{q} & \text{if} \quad \delta q_4 < 0 \end{cases} \tag{22}$$

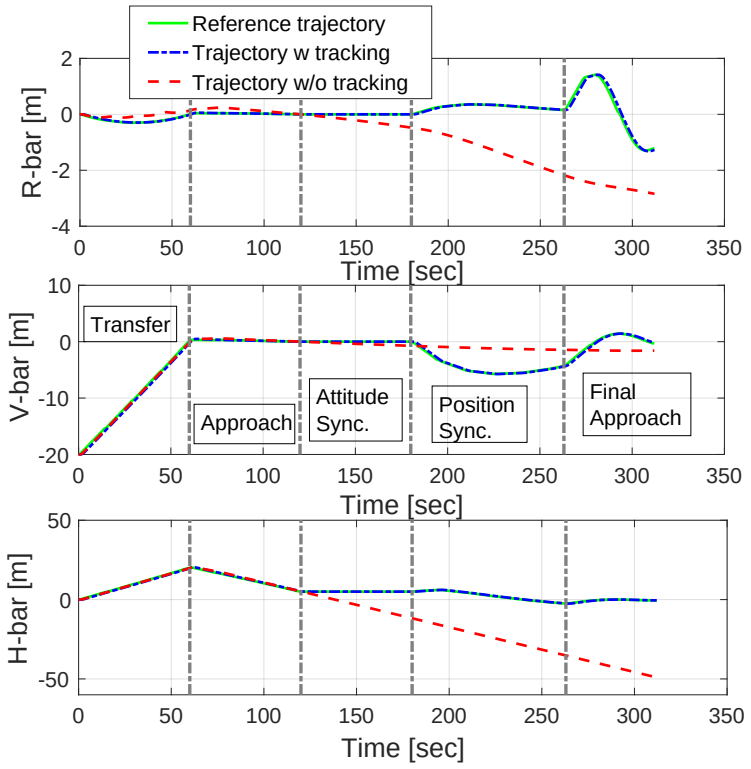

Fig. 5 Comparison of the reference trajectory calculated by the convex guidance system with simulation trajectories with and without tracking guidance system, referenced with respect to the Hill frame of the target spacecraft

The linear P controller of Eq. (19) tracks the error between the rate of the tumbling debris item, ω_T, and the chaser spacecraft, ω_C, and provides sufficient control to obtain rate synchronisation to a given threshold. This threshold, $\Delta\omega$, defines the discrete switching point from linear control to full state INDI control. It should be set to a sufficiently low value, here taken as 0.6 deg/s, to ensure that the angular velocities are nearly synchronised. Once switched, the full state INDI controller proposed in Ref. [17] is used. This implementation uses error kinematics based on the quaternion error vector, $\delta\mathbf{q}$, given by:

$$\delta\dot{\mathbf{q}} = \frac{1}{2}\left(\mathbf{Q}_1\omega_T - \mathbf{Q}_2\omega_C\right) \tag{23}$$

$$\mathbf{Q}_1 = \begin{bmatrix} \delta q_4 & -\delta q_3 & \delta q_2 \\ \delta q_3 & \delta q_4 & -\delta q_1 \\ -\delta q_2 & \delta q_1 & \delta q_4 \\ -\delta q_1 & -\delta q_2 & -\delta q_3 \end{bmatrix} \tag{24}$$

$$\mathbf{Q}_2 = \begin{bmatrix} \delta q_4 & \delta q_3 & -\delta q_2 \\ -\delta q_3 & \delta q_4 & \delta q_1 \\ \delta q_2 & -\delta q_1 & \delta q_4 \\ -\delta q_1 & -\delta q_2 & -\delta q_3 \end{bmatrix} \tag{25}$$

Furthermore, to allow for more rapid control, the Time Scale Separation principle is applied during the dynamic inversion and results in more effective attitude control. Consequently, the system inversion is applied twice, once to the attitude dynamics and once to the error quaternion kinematics. Subsequently, the two systems are coupled through the input for the outer-loop controller, which becomes the reference signal that the inner-loop controller must follow.

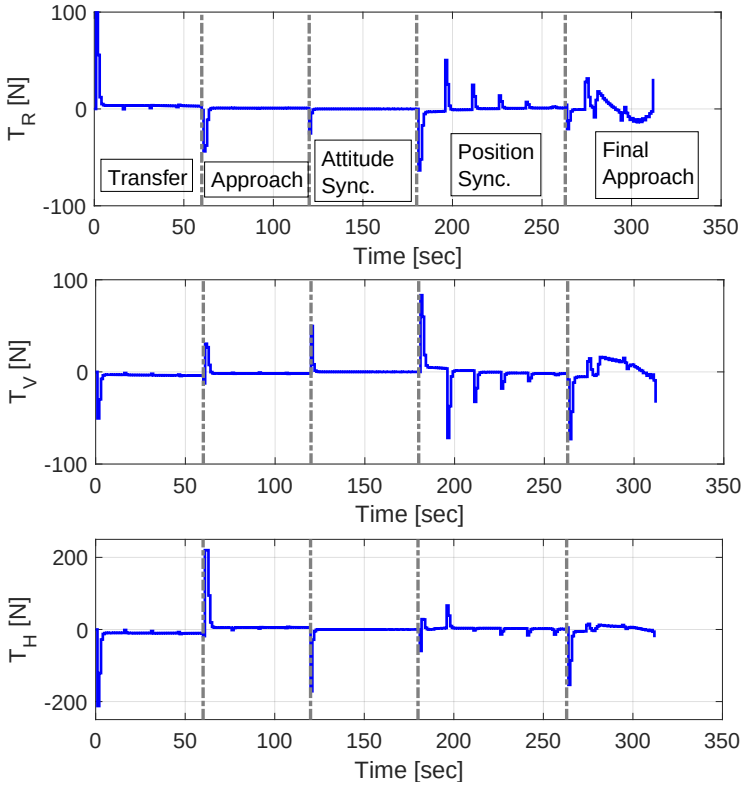

Fig. 6 Continuous thrust commands calculated by the combined guidance system, referenced with respect to the Hill frame of the target spacecraft

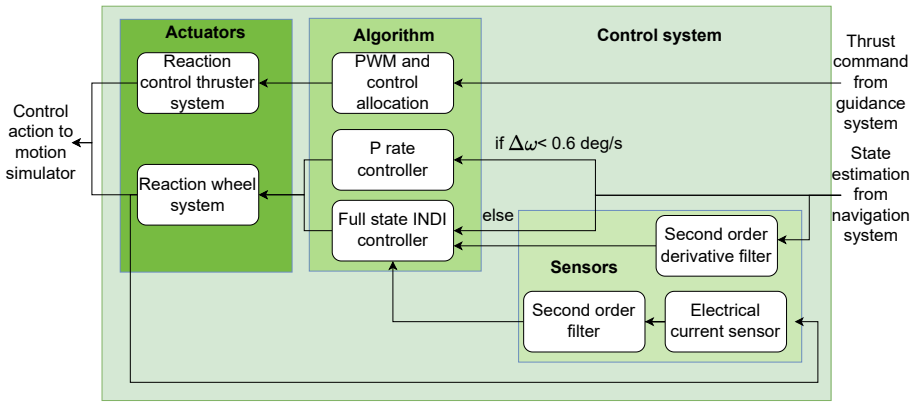

Fig. 7 Control system design

The inner-loop rate controller is given in Eq. (20) and tracks the desired angular velocity profile, $\boldsymbol{\omega}_{des}$, coming from the outer-loop attitude controller. Note that the system linearisation of this inner-loop controller resulted from an incremental control input that is added to the reference input, $\mathbf{M}_0$, and requires knowledge of the inertia tensor, $\mathbf{J}$, of the spacecraft along with angular acceleration measurements, $\dot{\boldsymbol{\omega}}_{meas}$. Furthermore, note that, for effective control, the time stamp of the reference input signal must correspond to that of the angular-acceleration measurements.

The outer-loop attitude controller is given by Eq. (21) and generates the required angular velocity profile for the inner-loop to track the attitude of the target spacecraft. In this equation, an orthogonal projection is applied by premultiplying $\Delta\mathbf{q}$ by $\mathbf{Q}_1\mathbf{Q}_1^T$, which ensures that the control action always remains feasible. The equation makes use of the quaternion tracking error, $\Delta\mathbf{q}$, and is defined in Eq. (22). Its value depends on the sign of the scalar part of the quaternion error vector, such that the outer-loop controller always rotates along the shortest way that reaches the desired

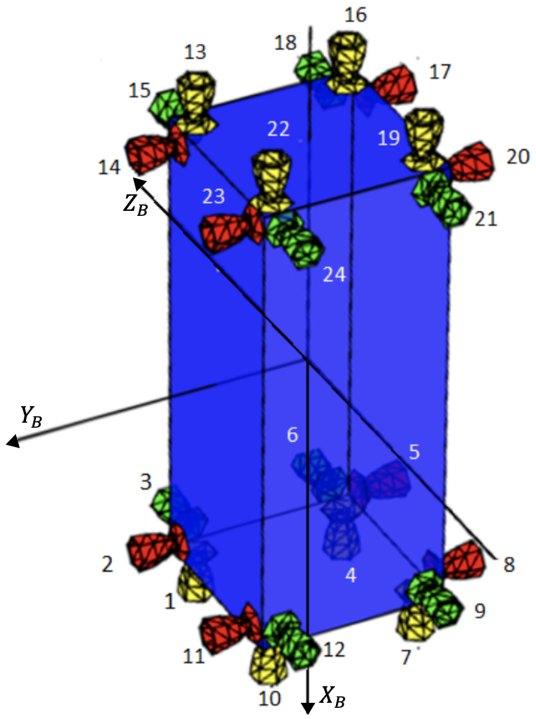

Fig. 8 Reaction-control thruster system configuration, adapted from [18]

attitude [17].

To control the state of the chaser spacecraft, it is equipped with two types of actuators. On one hand, control over the translational state is performed by a reaction-control thruster system, whereas on the other hand, a reaction-wheel system controls its rotational state.

For the reaction-control system to provide omnidirectional thrust, a configuration of 24 reaction-control thrusters, configured in pods of three thrusters on each vertex of the chaser's body, is used. A graphical representation of this configuration is given in Fig. 8.

An ideal but non-throttled model is applied to each reaction-control thruster. This reduces the controllability over the chaser spacecraft and therefore an algorithm is developed that effectively modulates the pulse-width of the thruster. Furthermore, to increase the efficiency of the control system, the algorithm will also allocate the commanded control actions over the different reaction-control thrusters. This allocation and modulation is formulated as an optimisation problem and is provided as Problem 3.

Problem 3:

$$\underset{\mathbf{t}_{act}}{\text{minimise}} \quad J_f = ||\mathbf{V}\mathbf{u} - \mathbf{u}_{cmd}|| + \varepsilon||\mathbf{u}|| \quad \text{subject to} \tag{26}$$

$$\mathbf{u} = \text{diag}\left(\mathbf{t}_{act}\right) T_{nom} \mathbf{1}_N^T \tag{27}$$

$$0 \leqslant t_{act_i} \leqslant \Delta t_{guid} \quad \forall i \in \{1, ..., N\} \tag{28}$$

The objective of Problem 3 is to minimise the discrepancy between the commanded control action, $\mathbf{u}_{cmd}$, and the provided control action. To calculate the provided control action, use is made of the configuration matrix of the actuators, $\mathbf{V}$, containing the positions and orientations of the different reaction-control thrusters in the spacecraft body frame. This configuration matrix can straightforwardly be established from Fig. 8. Furthermore, use is made of the control input vector provided by each of the actuators, $\mathbf{u}$. As the system represents a redundant control system, the objective function is extended with a secondary objective that minimises the required control effort, using the scaling parameter ε. This scaling parameter is generally set to a low value, $O(10^{-3})$, to prioritise control error over control effort minimisation [19]. Moreover, to ensure that the allocation algorithm simultaneously performs pulse-width modulation, the control input vector, $\mathbf{u}$, is linked to an activation time vector, $\mathbf{t}_{act}$, using Eq. (27). Note, however, that this activation

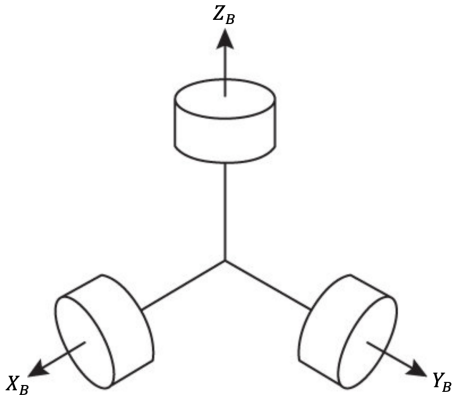

Fig. 9 Reaction-wheel system configuration, adapted from [21]

time vector, which contains an equal number of entries as there are reaction-control thrusters, is constrained by Eq. (28), such that an upper limit is imposed equal to the time step of the guidance function, Δt_{guid}. Lastly, it should be noted that the control allocation algorithm will provide an activation time that can be anywhere within the interval from 0 to Δt_{guid}. Therefore, the calculated activation times are rounded to the nearest multiple of the thrusters' operational frequency to ensure correct modulation.

The reaction-wheel system of the chaser spacecraft is modelled using three orthogonal wheels, as given in Fig. 9, and follows the parameterisation provided in [20]. Nevertheless, it should be noted that in contrast to [20], the reaction-wheels are assumed to be perfectly aligned. All other sources of noise, such as viscous and Coulomb friction, are however maintained. Furthermore note that, for redundancy purposes, it is recommended to use four wheels in a pyramid configuration. Nevertheless, to maintain simplicity, this has currently not been implemented and would require a straightforward modification to the configuration matrix characterising the reaction-wheels.

As discussed before, accurate measurements of the actuator output and spacecraft state are required at a sufficiently high sampling rate to be able to effectively apply the INDI technique as attitude controller of the spacecraft. Therefore, sensor models to obtain this information have been established and are detailed below. Note that for the current implementation, measurements of the angular acceleration of the chaser spacecraft and of the outputs generated by its actuators are needed. Dedicated sensors that measure angular accelerations exist, but are unlikely to be installed for an ADR mission. Therefore, accurate estimates of the angular accelerations will have to be deduced from noisy gyroscope measurements. To ensure that the signal-to-noise ratio does not decrease too much, it is first passed through a low pass filter. This will smooth the signal, before taking its derivative. The second-order low-pass filter proposed by [22] performs this combined action and can be defined as:

$$H(s) = \frac{\omega_n^2 s}{s^2 + 2\zeta\omega_n s + \omega_n^2} \tag{29}$$

Furthermore, to estimate the control moment generated by the reaction-wheels, a simple relation between the current drawn by the wheel and the generated control torque can be employed. Therefore, an electrical current sensor is modelled and contains a random noise value that is proportional the measured current. Note however that, to ensure that this actuator output measurement is synchronised in time with the acceleration measurement, it is required that the signal is filtered using an equivalent low-pass filter. This filtering will on one hand remove the noise from the signal, whereas on the other hand, it will ensure that the delay in the actuator output measurements is equal to the delay of the measured acceleration signal. As this delay is low compared to the time constant of the system dynamics, it will not further affect the controller's performance.

A summary of the parameter values defining the control system is provided in Table 2.

As a result of the provided attitude control system design, the performance of Fig. 10 can be obtained. In this figure, the angular velocity error and attitude error during synchronisation with a tumbling debris item are presented. It can be identified that, first the P rate controller is applied to reduce the angular velocity error to below the threshold, after which the full state INDI controller is used to achieve complete attitude synchronisation.

Moreover, the pulse-width modulation and control allocation algorithm transforms the thrust commands of the guidance system into control actions for the reaction-control thrusters. An example of the thrust outputs provided by

Table 2 Parameter values of control system

Threshold $\Delta\omega$ [deg/s]	0.6
Linear control gain K_p [-]	50
INDI control gain $K_{p,in}$ [-]	5
INDI control gain $K_{p,out}$ [-]	0.1
RCT thrust level T_{nom} [N]	55
RWA viscous friction coefficient [Nms]	$4.84 \cdot 10^{-6}$
RWA coulomb friction coefficient [Nm]	$8.975 \cdot 10^{-4}$
Low-pass filter ω_n [Hz]	50
Low-pass filter ζ [-]	0.55
Current sensor noise percentage [%]	0.5

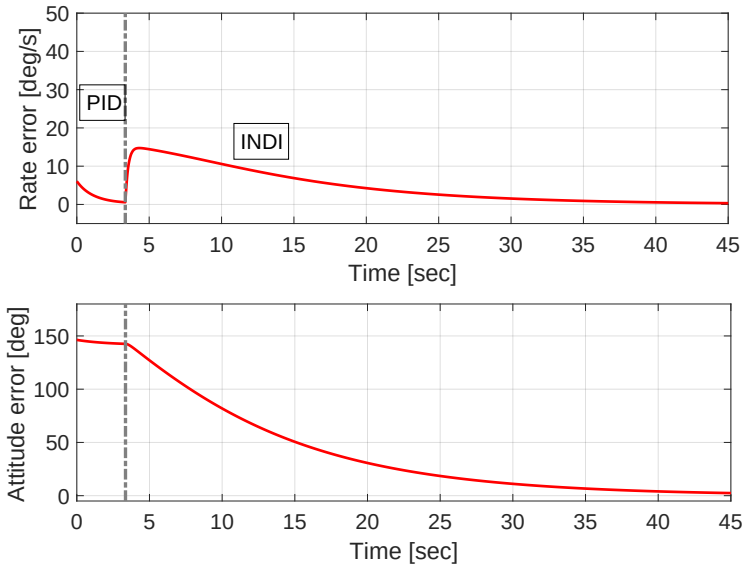

Fig. 10 Angular rate error (top) and attitude error (bottom) during synchronisation with tumbling debris item performed by integrated attitude control system

three of the omnidirectional thrusters is given in Fig. 11. This figure showcases that the algorithm accurately translates the continuous thrust inputs of the guidance system, previously given in Fig. 6, into discrete pulses of the non-throttled thrusters.

Note that the performance in the provided figures is obtained by the integrated attitude control system, using the described models for the control sensors and actuators.

VI. Navigation System

The navigation system onboard the current ADR mission is tasked with performing inertial state estimation of the chaser spacecraft, along with relative state estimation of its target. A summary of the developed system is provided in Fig. 12, from which it can be seen that a conventional Unscented Kalman Filter (UKF) is implemented for inertial navigation, in combination with an artificial Vision-based Navigation (VBN) system for relative navigation. To cover the inertial state estimation of the translational and rotational state of the chaser spacecraft, the current paper employs measurements from an IMU, a GPS receiver and a star sensor. The implemented IMU model is based on [23] and contains bias, scaling, and misalignment factors, and white-noise errors for each acceleration and angular velocity component. Moreover, to obtain GPS receiver measurements, a sensor model is developed that contains white-noise in range and range rate measurements, along with clock bias and clock drift errors. Lastly, the star sensor model given by [24] is implemented and contains a white-noise error in each measured attitude component.

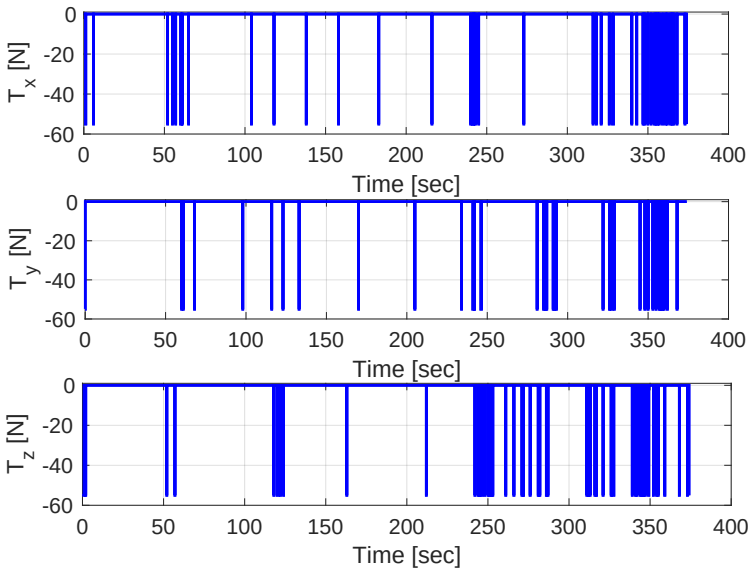

Fig. 11 Reaction-control thruster output of thruster 1 (top), thruster 2 (middle) and thruster 3 (bottom), referenced with respect to the body frame of the chaser spacecraft

The framework of the UKF is centred around the state estimation of a discrete-time nonlinear system, as given by:

$$\mathbf{x}_{k+1} = f(\mathbf{x}_k, \mathbf{u}_k, \mathbf{v}_k) \tag{30}$$

$$\mathbf{y}_{k+1} = g(\mathbf{x}_{k+1}, \mathbf{w}_{k+1}) \tag{31}$$

In Eq. (30), $\mathbf{x}$ represents the state vector, $\mathbf{u}$ the control input vector, $\mathbf{v}$ the process-noise vector and $f()$ the nonlinear dynamics. Furthermore, in Eq. (31), $\mathbf{y}$ represents the measurement vector, $\mathbf{w}$ the observation noise vector and $g()$ the nonlinear measurement function. Using this system dynamics, the UKF performs an a-priori state and covariance estimate and subsequently applies an a-posteriori correction using sensory measurements. By applying these prediction and correction steps sequentially, a more accurate estimate of the spacecraft state can be obtained.

A summary of the a-priori state estimation principle is provided in Problem 4.

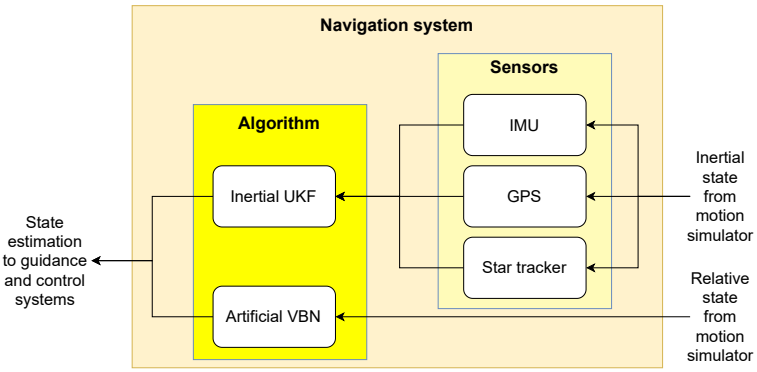

Fig. 12 Navigation system design

Problem 4:

$$\boldsymbol{\chi}_0^k = \hat{\mathbf{x}}_k \tag{32}$$

$$\boldsymbol{\chi}_i^k = \hat{\mathbf{x}}_k + \left(\sqrt{(L+\lambda)}\sqrt{\hat{\mathbf{P}}_{x_i}^k}\right) \qquad \text{for } i = 1, ..., L \tag{33}$$

$$\boldsymbol{\chi}_i^k = \hat{\mathbf{x}}_k - \left(\sqrt{(L+\lambda)}\sqrt{\hat{\mathbf{P}}_{x_{i-L}}^k}\right) \qquad \text{for } i = L, ..., 2L \tag{34}$$

$$\lambda = \alpha^2(L+\kappa) - L \tag{35}$$

$$\boldsymbol{\chi}_i^{k+1} = f(\boldsymbol{\chi}_i^k, \mathbf{u}_k, \mathbf{v}_k) \qquad \text{for } i = 0, ..., 2L \tag{36}$$

$$\overline{\mathbf{x}}_{k+1} = \sum_{i=0}^{2L} \left(W_i{}^m \boldsymbol{\chi}_i^{k+1}\right) \tag{37}$$

$$\overline{\mathbf{P}}_x^{k+1} = \sum_{i=0}^{2L} W_i{}^c \left(\boldsymbol{\chi}_i^{k+1} - \overline{\mathbf{x}}_{k+1}\right)\left(\boldsymbol{\chi}_i^{k+1} - \overline{\mathbf{x}}_{k+1}\right)^T + \mathbf{Q} \tag{38}$$

$$W_0{}^m = \frac{\lambda}{L+\lambda} \tag{39}$$

$$W_0{}^c = \frac{\lambda}{L+\lambda} + \left(1 - \alpha^2 + \beta\right) \tag{40}$$

$$W_i{}^m = W_i{}^c = \frac{1}{2\,(L+\lambda)} \qquad \text{for } i = 1, ..., 2L \tag{41}$$

In these equations, $\boldsymbol{\chi}_i^k$ represent sigma-point vectors, which populate a deterministically selected cloud of weighted points around the state estimate, $\hat{\mathbf{x}}_k$. In total, $2L + 1$ sigma-point vectors are calculated, where L represents the number of states in the state vector. These sigma-point vectors can be obtained from Eqs. (32) to (34) and use the i^{th} row of the matrix square root of the state covariance matrix, $\sqrt{\hat{\mathbf{P}}_{x_i}^k}$, and a scaling parameter, λ, given by Eq. (35). Note that this scaling parameter is defined by α, which determines the spread of the sigma-points around the mean and usually set to a small value, $O\left(10^{-3}\right)$, κ, which is a secondary scaling parameter and generally set to 0, and β, a parameter used to incorporate knowledge on the distribution of the to-be-estimated state vector. For Gaussian distributions, an optimal value for β is set at 2. Subsequently, these sigma-point vectors are propagated through the nonlinear system dynamics, as given by Eq. (36), and an a-priori state and state covariance matrix estimate, $\overline{\mathbf{x}}_{k+1}$ and $\overline{\mathbf{P}}_x^{k+1}$, respectively, can be calculated using Eqs. (37) and (38). Note that these latter two equations make use of weight factors, W^m and W^c, provided by Eqs. (39) to (41). Moreover, Eq. (38) includes the process-noise covariance matrix $\mathbf{Q}$.

These propagated sigma-point vectors are subsequently used to obtain an a-posteriori state correction based on performed measurements, as given in Problem 5.

Problem 5:

$$\overline{\mathbf{y}}_{k+1} = \sum_{i=0}^{2L} \left(W_i{}^m \boldsymbol{\Upsilon}_i^{k+1}\right) \tag{42}$$

$$\overline{\mathbf{P}}_y^{k+1} = \sum_{i=0}^{2L} W_i{}^c \left(\boldsymbol{\Upsilon}_i^{k+1} - \overline{\mathbf{y}}_{k+1}\right)\left(\boldsymbol{\Upsilon}_i^{k+1} - \overline{\mathbf{y}}_{k+1}\right)^T + \mathbf{R} \tag{43}$$

$$\boldsymbol{\Upsilon}_i^{k+1} = g\left(\boldsymbol{\chi}_i^{k+1}, \mathbf{w}_{k+1}\right) \qquad \text{for } i = 0, ..., 2L \tag{44}$$

$$\mathbf{P}_{xy}^{k+1} = \sum_{i=0}^{2L} W_i{}^c \left(\boldsymbol{\chi}_i^{k+1} - \overline{\mathbf{x}}_{k+1}\right)\left(\boldsymbol{\Upsilon}_i^{k+1} - \overline{\mathbf{y}}_{k+1}\right)^T \tag{45}$$

$$\mathbf{K}_{k+1} = \mathbf{P}_{xy}^{k+1}\left(\overline{\mathbf{P}}_y^{k+1}\right)^{-1} \tag{46}$$

$$\hat{\mathbf{x}}_{k+1} = \overline{\mathbf{x}}_{k+1} + \mathbf{K}_{k+1}\left(\mathbf{y}_{k+1} - \overline{\mathbf{y}}_{k+1}\right) \tag{47}$$

$$\hat{\mathbf{P}}_x^{k+1} = \overline{\mathbf{P}}_x^{k+1} - \mathbf{K}_{k+1}\overline{\mathbf{P}}_y^{k+1}\left(\mathbf{K}_{k+1}\right)^T \tag{48}$$

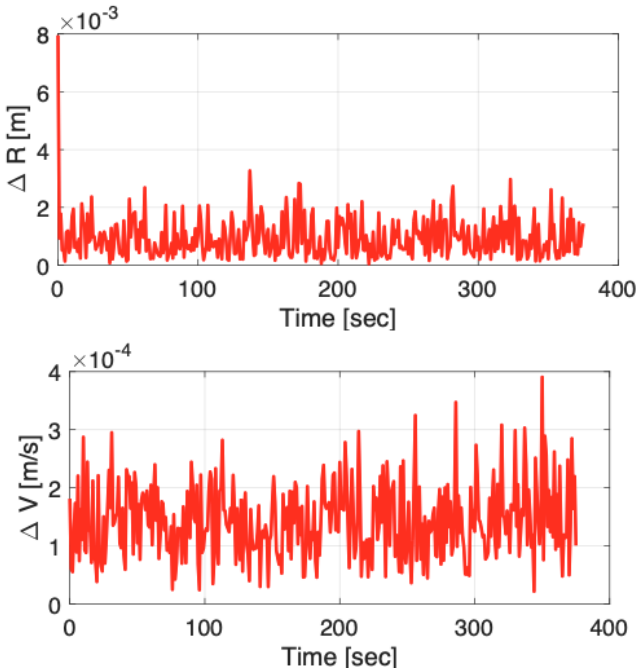

Fig. 13 Inertial navigation errors in position estimation (top) and velocity estimation (bottom) provided by the Unscented Kalman filter

First, the measurement vector, $\overline{\mathbf{y}}_{k+1}$, and its corresponding covariance matrix, $\overline{\mathbf{P}}_{y}^{k+1}$, are estimated using Eqs. (42) and (43). In these equations, the previously established weight factors are used along with the transformed sigma-point vectors through the nonlinear measurement equation, $\boldsymbol{\Upsilon}_{i}^{k+1}$, as given by Eq. (44). Moreover, Eq. (43) includes the measurement-noise covariance matrix $\mathbf{R}$.

Note that the process-noise covariance matrix, $\mathbf{Q}$, and the measurement-noise covariance matrix, $\mathbf{R}$, have been manually tuned, such that the true navigation error of the UKF remains closely bounded by its estimated navigation error.

Following this, the cross-covariance matrix, $\mathbf{P}_{xy}^{k+1}$, can be estimated, as given in Eq. (45). Lastly, the calculated estimates can be corrected using the performed measurements, given by the true measurement vector $\mathbf{y}_{k+1}$. This step is identical to the correction step performed in a classical Kalman filter. Therefore, the Kalman gain can be directly calculated from Eq. (46), and the a-posteriori estimate of the state and its covariance matrix can be calculated from Eqs. (47) and (48), respectively.

A summary of the parameter values defining the inertial navigation system is provided in Table 3. Note that, as the inertial navigation system simultaneously estimates the chaser's position, velocity, IMU accelerometer bias, GPS receiver clock bias and drift, inertial attitude and angular velocity, it's estimation consists of 18 states. Furthermore, note that to estimate these states, the inertial navigation system uses range and range rate measurements that are obtained with respect to four GPS satellites, one quaternion measurement from the star tracker and one angular velocity vector measurement from the IMU's gyroscope.

The performance of the inertial UKF filter results in the state estimation errors given in Figs. 13 and 14. Note that as the error norms of the translational and rotational state estimation are provided, the corresponding bounding curves based on state error covariance matrices cannot be drawn. Nevertheless, it has been assessed and verified that the true estimation error is of the same magnitude as the expected error for all components.

The artificial vision-based navigation system is modelled using simple additive white-noise given by:

$$\mathbf{x}_{VBN} = \mathbf{x}_{rel} + \boldsymbol{\nu}_{VBN} \tag{49}$$

In this equation, $\mathbf{x}_{VBN}$ represents the relative state estimate that is outputted by the artificial navigation filter, $\mathbf{x}_{rel}$ the true relative state between both spacecraft, and $\boldsymbol{\nu}_{VBN}$ a random white noise vector representing the state estimation errors. Note that the magnitude of the white noise vector is directly proportional to the true relative state and contains a distinct white noise value for each component. A mathematical description of this white noise vector is given by:

Table 3 Parameter values of inertial navigation system

UKF initial state covariance $\hat{P}_x^0$ [-]	$\mathbf{I_{18\times 18}}$
UKF process-noise covariance Q [-]	$\text{diag}(\begin{bmatrix} 4\cdot 10^{-5}\mathbf{I_{3\times 3}} \\ 0.25\cdot 10^{-5}\mathbf{I_{3\times 3}} \\ 10^{-6}\cdot \mathbf{I_{3\times 3}} \\ 10^{-10}\cdot \mathbf{I_{2\times 2}} \\ 0.0071, 00084, \\ 0.0094, 0.0154 \\ 6\cdot 10^{-4} \end{bmatrix})$
UKF measurement-noise covariance R [-]	$\text{diag}(\begin{bmatrix} 10^{-5}\mathbf{I_{4\times 4}} \\ 10^{-7}\mathbf{I_{4\times 4}} \\ 10^{-14}\cdot \mathbf{I_{4\times 4}} \\ 10^{-9}\cdot \mathbf{I_{3\times 3}} \end{bmatrix})$
IMU accelerometer misalignment and scale factors [-]	$\begin{bmatrix} 1.0002 & 10^{-6} & -10^{-6} \\ -10^{-6} & 0.99983 & 2\cdot 10^{-6} \\ 10^{-6} & 2\cdot 10^{-6} & 1.00023 \end{bmatrix}$
IMU accelerometer bias [m/s2]	$\begin{bmatrix} 3\cdot 10^{-4} \\ -3.5\cdot 10^{-4} \\ 3\cdot 10^{-4} \end{bmatrix}$
IMU accelerometer noise [m/s2]	10^{-5}
IMU gyroscope misalignment and scale factors [-]	$\begin{bmatrix} 1.0002 & 10^{-6} & -10^{-6} \\ -10^{-6} & 0.99983 & 2\cdot 10^{-6} \\ 10^{-6} & 2\cdot 10^{-6} & 1.00023 \end{bmatrix}$
IMU gyroscope bias [rad/s]	$\begin{bmatrix} 5\cdot 10^{-6} \\ -5\cdot 10^{-6} \\ 5\cdot 10^{-6} \end{bmatrix}$
IMU gyroscope noise [rad/s]	10^{-6}
GPS clock bias [m]	1
GPS clock drift [m/s]	0.1
GPS range noise [m]	0.03
GPS range rate noise [m/s]	0.001
Star sensor noise [-]	$2.5\cdot 10^{-6}$

Table 4 Parameter values of relative navigation system

VBN position noise percentage [%]	$\frac{\sqrt{3}}{9}$
VBN velocity noise percentage [%]	$\frac{\sqrt{3}}{9}$
VBN attitude noise percentage [%]	$\frac{1}{6}$
VBN angular rate noise percentage [%]	$\frac{\sqrt{3}}{9}$

$$\boldsymbol{\nu}_{VBN} \sim N(0, p_{\%}||\mathbf{x}_{rel}||) \tag{50}$$

where $\boldsymbol{\nu}_{VBN}$ is sampled from a normal distribution $N()$, characterised by a zero mean and a standard deviation equal to a predefined percentage $p_{\%}$ of the magnitude of the actual relative state vector $||\mathbf{x}_{rel}||$.

A summary of the parameter values defining this relative navigation system is provided in Table 4. For brevity purposes, no further results will be provided regarding this artificial relative navigation system.

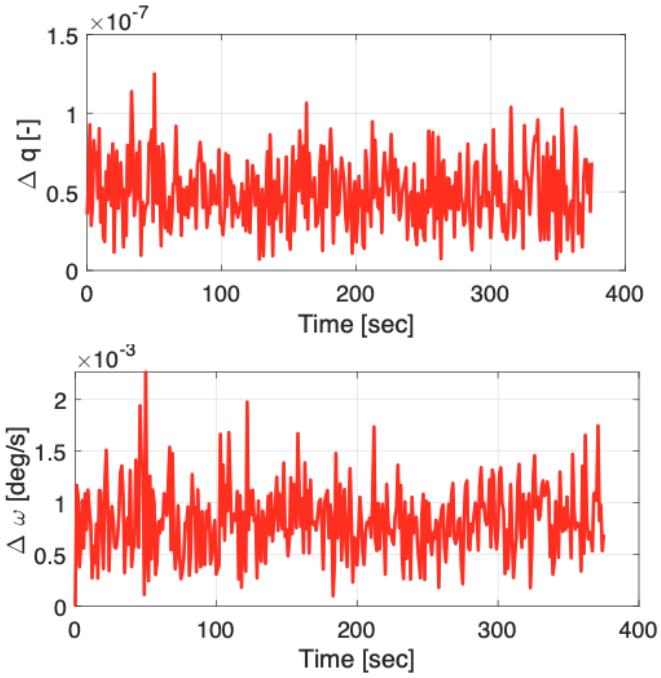

Fig. 14 Inertial navigation errors in quaternion estimation (top) and rate estimation (bottom) provided by the Unscented Kalman filter

VII. Results

The individual guidance, navigation, and control subsystems, as detailed above, have subsequently been integrated into one GNC system. With this GNC system, the flight trajectory of Fig. 15 can be obtained. Note that for comparison, this and future figures will also provide the trajectories obtained when using an isolated guidance system and an integrated guidance and control system.

For all three trajectory calculations, identical environmental disturbances are implemented. Trajectory dispersions grow as the integrated system becomes more realistic, such that the guidance system is required to perform more frequent recalculations. This implies that differences in the flown trajectories, although partly caused by errors in the control and/or navigation systems, cannot solely be quantified as trajectory errors. This is because the guidance system continuously reconstructs the optimal path to the capture position using its current state as initial condition. Consequently, performing a direct trajectory comparison is difficult. Nevertheless, it is visible from Fig. 15 that similar trajectories are flown for the three levels of GNC-system complexity.

Conversely, to achieve these seemingly analogous trajectories, three rather different thrust input histories are calculated, as can be seen from Fig. 16. Once again, differences in these thrust profiles are due to recalculations performed by the guidance system.

Moreover, for the integrated guidance and control system and the integrated GNC system, these thrust commands are allocated over the available reaction control thrusters and subsequently modulated. The result of this procedure is given in Fig. 17 for three of the thrusters. From this figure it can be observed that the thrusters either provide no thrust, or short pulses of thrust at maximum capacity, indicating a correctly functioning modulation and allocation algorithm. Furthermore, it can be observed from the trajectories in Fig. 15 and the previously provided discussion that, the modulation and allocation algorithm provides sufficient controllability over the translational state of the chaser spacecraft.

Additionally, the integrated guidance and control system, and the integrated GNC system provide attitude synchronisation with the tumbling debris item. To compare their respective results, Fig. 18 can be employed. In this figure, the angular velocity error and the attitude error during the entire mission duration are provided. The system response of both systems is near-identical, even though the integrated guidance and control system uses ideal navigation measurements as input, whereas the integrated GNC system employs the state estimates of the navigation system.

Once more, the calculated control inputs of both system are rather different, as can be seen from Fig. 19. In this

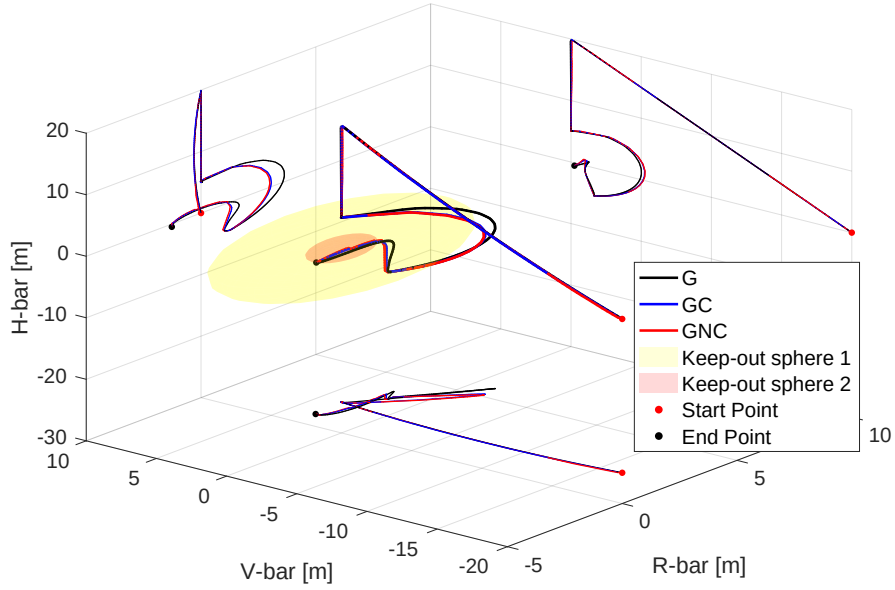

Fig. 15 Trajectories flown by isolated guidance system (G), integrated guidance and control system (GC) and integrated GNC system (GNC), as expressed in the Hill frame of the target spacecraft and containing keep-out sphere constraints

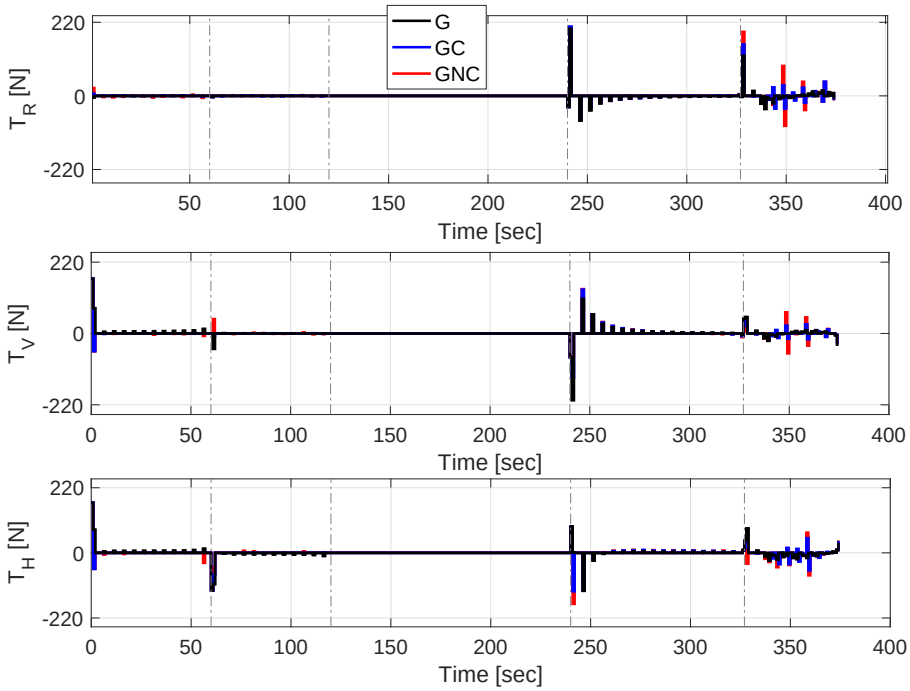

Fig. 16 Thrust vector components calculated by the guidance system referenced with respect to the Hill frame of the target spacecraft

figure, the control moment components provided by the reaction wheel system are presented. It can be identified that a larger moment is required for the integrated GNC system and that the time history of this control moment is less smooth. This is caused by the errors present in the navigation estimates and follows expectations. Still, the calculated control input remains bounded over the entire manoeuvre and, after the initial spikes at the instant the control systems are turned

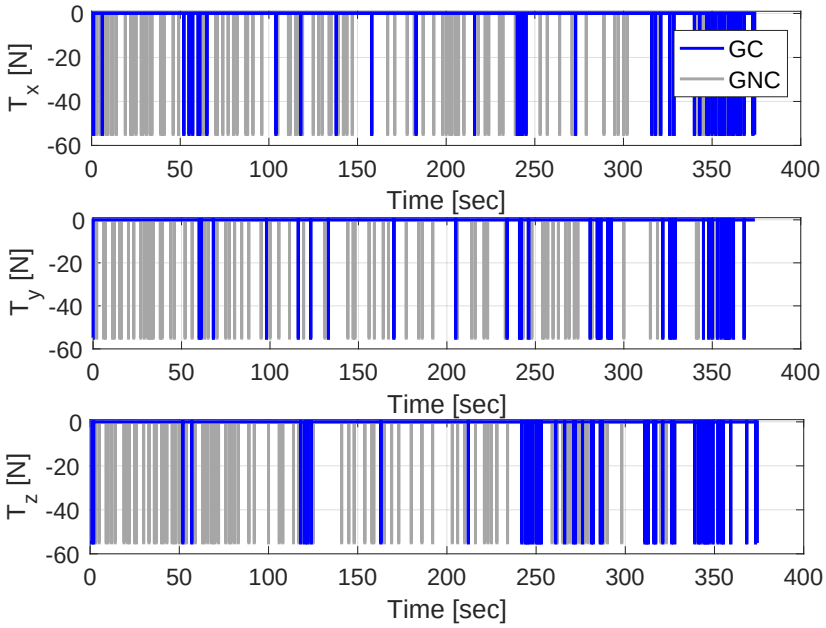

Fig. 17 Reaction control thruster output of thruster 1 (top), thruster two (middle) and thruster three (bottom), referenced with respect to the body frame of the chaser spacecraft

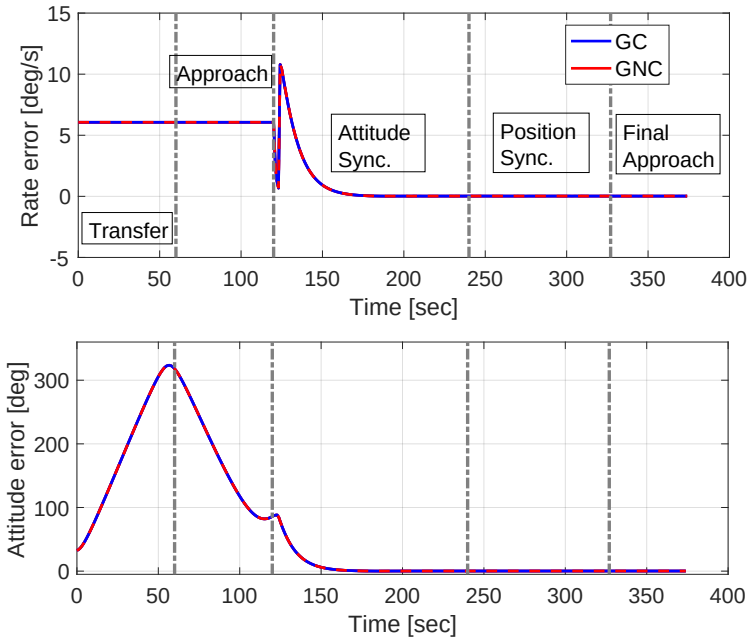

Fig. 18 Angular rate error (top) and attitude error (bottom) during synchronisation with tumbling debris item performed by integrated guidance and control system and integrated GNC system

on, the input history rapidly converges to a smooth tracking profile.

This integrated GNC system design results in the overall system performance given in Table 5, where the ADR mission is evaluated in terms of the terminal position dispersion with respect to the capture position, along with the required propellant consumption.

From this table it can be seen that both the terminal-position error and required fuel consumption grow proportionally to the magnitude of the target's angular velocity vector. This emerges from the fact that higher spin rates will result

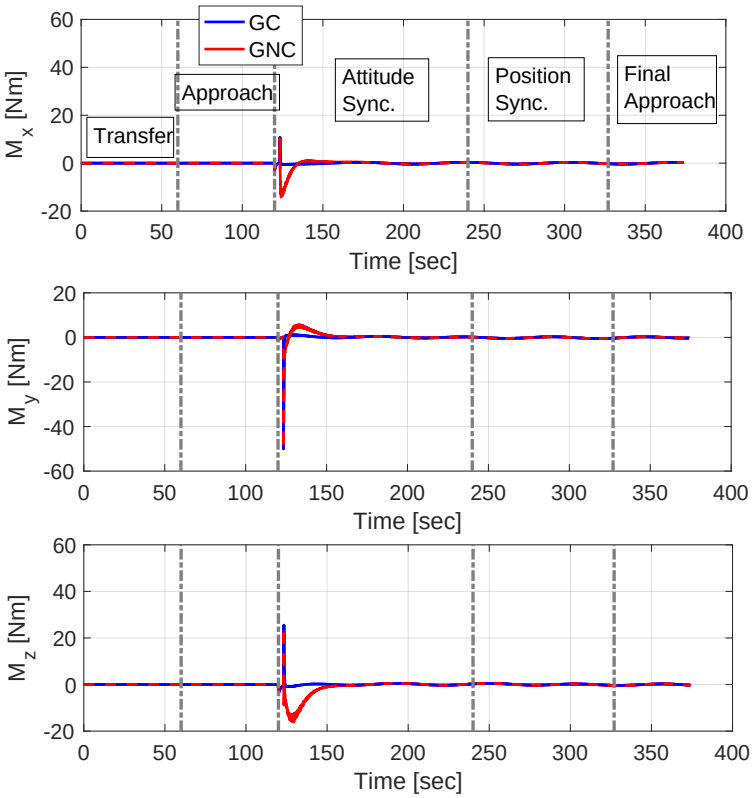

Fig. 19 Control input history during synchronisation with tumbling debris item performed by integrated guidance and control system and integrated GNC system

Table 5 Terminal position dispersion and fuel consumption for trajectories flown by integrated GNC system

Initial ω target [deg/s]	Position Error [cm]	Propellant mass [kg]
$(0,0,0)^T$	4.2	0.943
$(3.5,3.5,3.5)^T$	8.0	1.204
$(5,5,0)^T$	9.7	1.319
$(0,20,0)^T$	27.9	1.425

in more complex trajectories for the guidance system, requiring additional propellant to track the rapidly tumbling docking-axes. Furthermore, given the increasingly complex nature of these trajectories, GNC errors will accumulate in larger trajectory dispersions with respect to the capture position. Therefore, the results provided in Table 5 are in line with expectations. Moreover, it can be observed that all terminal-position errors remain low, far below 50 cm, while requiring limited propellant, *i.e.*, less than 1.5 kg.

In addition to analysing the performance of the GNC system, its robustness is examined using varying mission conditions. To this extent, the orientation of the docking-axis in the body frame of the target is altered to ensure flexibility of the developed GNC system to an in-orbit redefinition of the mission. This redefinition can be triggered from a visual inspection of the target prior to initiation of the close-range rendezvous phase, due to varying lighting conditions, communication availability, or contingencies in the mechanical state of the rocket body, which are all difficult to assess from ground. Therefore, fourteen different docking-axis definitions in a symmetrical distribution around the conical body of the target are analysed. A graphical description of these docking-axes is provided in Fig. 20, along with the terminal-position error and the propellant consumption that result from approaching the target along a particular docking-axis. When inspecting the variation in terminal-position error, it can be seen that this is limited to 1 cm. When putting this into perspective with the full scale of the close-range rendezvous phase, it can be concluded that this variation is negligible. However, a larger variation in propellant consumption can be observed. This is because the

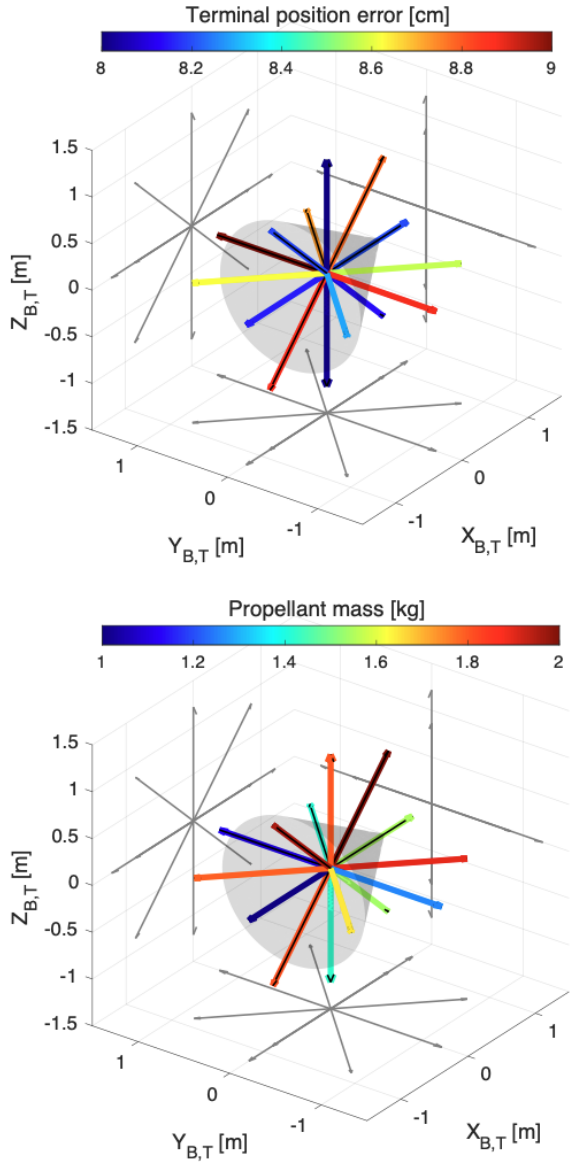

Fig. 20 Terminal-position error (top) and propellant consumption (bottom) obtained during docking-axis variation for a rotating target at $(3.5, 3.5, 3.5)^T$ deg/s. Note that the grey cone represents the conical rocket body and the arrows indicate the respective definitions of the docking-axes in the target body frame.

docking-axis needs to be closely followed during the two most complex mission segments of the close-range rendezvous, *i.e.*, the synchronisation phase and final approach phase. Therefore, a change in its definition will evidently alter the last part of the flown trajectories, resulting in large propellant variations. Nevertheless, as the terminal-position error hardly changes, it showcases how powerful the recalculation and correction actions of the GNC system are, and that the developed system is robust to changes in the flown mission scenario.

VIII. Conclusions

This paper presents a successfull GNC system design for an ADR mission to a defunct upper rocker body in LEO orbit. In particular, it showcases a robust and autonomous GNC system capable of executing the final rendezvous phase between an active chaser spacecraft and a passive debris item. The system is capable of handling a large variation of mission scenarios, characterised by different tumbling rates for the target spacecraft. Furthermore, the system is capable

of handling in-orbit redefinitions of the planned mission scenario, demonstrated by the dispersion of the approach directions over the docking axis. Despite all these variations, the GNC system remains capable of executing the mission by achieving a terminal position accuracy at centimeter level, while using a limited amount of propellant.

As the developed guidance algorithm does not include any specifics of the defunct rocket body in its formulation of the guidance problem, it is sufficiently generic to enable any ADR mission. Not only rocket bodies can be targeted, but also defunct satellites when a dedicated constraint is added to take care of their flexible appendages.

References

[1] Kessler, D., and Cour-Palais, B., "Collision frequency of artificial satellites: The creation of a debris belt," *Journal of Geophysical Research*, Vol. 83, 1978, pp. 2637–2646.

[2] Eichler, P., and Rex, D., "Chain reaction of debris generation by collisions in space - a final threat to spaceflight?" *Acta Astronautica*, Vol. 22, 1990, pp. 381–387.

[3] Liou, J., and Johnson, N., "A sensitivity study of the effectiveness of active debris removal in LEO," *Acta Astronautica*, Vol. 64, No. 2-3, 2009, pp. 236–243.

[4] Branco, J., Colmenarejo, P., Serra, P., Lourenço, P., Peters, T., and Mammarella, M., "Critical GNC Aspects for ADR missions," *Proceedings of the 11th International ESA Conference on Guidance, Navigation & Control Systems*, Virtual, June 22-25, 2021.

[5] Bonnal, C., Ruault, J., and Desjean, M., "Active debris removal: Recent progress and current trends," *Acta Astronautica*, Vol. 85, 2013, pp. 51–60.

[6] Estable, S., Pruvost, C., Ferreira, E., Telaar, J., Fruhnert, M., Imhof, C., Rybus, T., Peckover, G., Lucas, R., Ahmed, R., Oki, T., Wygachiewicz, M., Kicman, P., Lukasik, A., Santos, N., Milhano, T., Arroz, P., Biesbroek, R., and Wolahan, A., "Capturing and deorbiting Envisat with an Airbus Spacetug. Results from the ESA e.Deorbit consolidation phase study," *Journal of Space Safety Engineering*, Vol. 7, No. 1, 2020, pp. 52–66.

[7] Biesbroek, R., Aziz, S., Wolahan, A., Cipolla, S., Richard-Noca, M., and Piguet, L., "The ClearSpace-1 mission: ESA and clearspace team up to remove debris," *Proceedings of the 8th European Conference on Space Debris*, Virtual, March 20-23, 2021.

[8] Blackerby, C., Okamoto, A., Fujimoto, K., and Okada, N., "ELSA-D: An In-Orbit End-Of-Life Demonstration Mission," *Proceedings of the 69th International Astronautical Congress*, Bremen, Germany, October 1-5, 2018.

[9] Astroscale, "Astroscale's ADRAS-J Mission Starts Rendezvous Operations," [Online], 2024. Available: `https://astroscale.com/astroscales-adras-j-mission-starts-rendezvous-operations/` (Accessed 14 May 2024)).

[10] Leomanni, M., Quartullo, R., Bianchini, G., Garulli, A., and Giannitrapani, A., "Variable-Horizon Guidance for Autonomous Rendezvous and Docking to a Tumbling Target," *Journal of Guidance, Control and Dynamics*, Vol. 45, No. 5, 2022, pp. 846–858.

[11] Corpino, S., Mauro, S., Pastorelli, S., Stesina, F., Biondi, G., Franchi, L., and Mohtar, T., "Control of a Noncooperative Approach Maneuver Based on Debris Dynamics Feedback," *Journal of Guidance, Control, and Dynamics*, Vol. 41, 2017, pp. 1–18.

[12] ClearSpace SA, "ClearSpace - A mission to make space sustainable," [Online], 2022. Available: `https://clearspace.today` (Acessed 13 June 2022).

[13] Elecnor Deimos, "CLEARSPACE - Elecnor Deimos," [Online], 2020. Available: `https://elecnor-deimos.com/clearspace/` (Accessed 11 May 2024)).

[14] Efimov, S., Pritykin, D., and Sidorenko, V., "Defunct Satellites in Nearly Polar Orbits: Long-term Evolution of Attitude Motion," *Baltic astronomy an international journal*, Vol. 27, 2018, pp. 264–277.

[15] Hill, G., "Researches in the Lunar Theory," *American Journal of Mathematics*, Vol. 1, No. 1, 1878, pp. 5–26.

[16] Singh, S., Mooij, E., and Gransden, D., "Multibody Approach to the Controlled Removal of Large Space Debris with Flexible Appendages," *Proceedings of the 2019 AIAA Scitech Forum*, San Diego, CA, January 7-11, 2019.

[17] Bacon, B., "Quaternion-Based Control Architecture for Determining Controllability/Maneuverability Limits," *Proceedings of the 2012 AIAA Guidance, Navigation, and Control Conference*, Minneapolis, MN, August 13-16, 2012.

[18] Habets, J., Mooij, E., and Frost, S., "Evolving Systems Approach to the Attitude Control of a Space-Debris Removal Spacecraft," *Proceedings of the 2017 AIAA Guidance, Navigation, and Control Conference*, Grapevine, TX, January 9-13, 2017.

[19] Bodson, M., and Frost, S., "Load Balancing in Control Allocation," *Journal of Guidance, Control, and Dynamics*, Vol. 34, 2011, pp. 380–387.

[20] Carrara, V., and Kuga, H., "Estimating Friction Parameters in Reaction Wheels for Attitude Control," *Mathematical Problems in Engineering*, Vol. Vol. 2013, 2013.

[21] Narkiewicz, J., Sochacki, M., and Zakrzewski, B., "Generic Model of a Satellite Attitude Control System," *International Journal of Aerospace Engineering*, Vol. 2020, 2020, pp. 1–17.

[22] E. Smeurs, "Incremental Control of Hybrid Micro Air Vehicles," Ph.D. thesis, Delft University of Technology, 2018.

[23] Mooij, E., and Chu, Q., "IMU/GPS Integrated Navigation System for a Winged Re-entry Vehicle," *Proceedings of the 2001 AIAA Guidance, Navigation, and Control Conference*, Montreal, Canada, August 6-9, 2001.

[24] Canuto, E., Novara, C., Massotti, L., Perez Montenegro, C., and Carlucci, D., *Spacecraft dynamics and control: the Embedded Model Control approach*, Elsevier, Amsterdam, the Netherlands, 2018.